



AIAA 2001-0650

CFD Simulation of a 2-KW Class Laser Thruster

P. Molina-Morales, K. Toyoda, K. Komurasaki, Y. Arakawa

University of Tokyo

Japan

38th Aerospace Sciences Meeting & Exhibit

10-13 January 2001

Reno, Nevada

CFD SIMULATION OF A 2-KW CLASS LASER THRUSTER

P. Molina-Morales*, K. Toyoda*, K. Komurasaki†, and Y. Arakawa‡
University of Tokyo, Hongo 7-3-1, Bunkyo, Tokyo 113-0033, Japan

ABSTRACT

Laser propulsion powered by a CW laser has been studied. Thruster performance and energy balance in the thruster were numerically computed. Laser beam optics, inverse-bremsstrahlung absorption, ionization/recombination reactions, radiation, heat conduction, and convection have been modeled. Computational stiffness due to the very small flow speed has been overcome by using a Flux Vector Splitting implicit scheme with a large CFL number. The computed positions of the Laser Sustained Plasma (LSP) in the thruster show good agreement with the measured ones. The estimated energy conversion efficiency was 23%, and the rest of the input power was lost as radiation from the LSP and also carried by the laser beam passing through the LSP.

NOMENCLATURE

C_F : thrust coefficient
 D : diffusion coefficient
 D_t : throat diameter
 E : total energy
 f : ratio of focal length to incident beam diameter
 F, G : numerical flux vectors in the axial and radial directions
 h : heat of formation
 I : laser intensity
 k : Boltzmann's constant
 K : inverse bremsstrahlung coefficient
 M : mass of a heavy particle

n : number density
 p : pressure
 P : incident laser power
 q : laser absorption rate
 R : gas constant
 t : time
 T : temperature, or thrust
 u : velocity in the axial direction
 U : vector of characteristic variables
 v : velocity in the radial direction
 V_j : exhaust velocity
 w : beam radius
 W : vector of source terms
 x, y : coordinates in the axial and radial directions
 γ : specific heat ratio
 η_E : energy conversion effic. as given by Eq. (17)
 η_T : energy conversion effic. as given by Eq. (16)
 κ : thermal conductivity
 λ : laser wavelength
 ν : collision frequency
 ρ : density
 τ : viscosity
 ω : reaction rate

1. INTRODUCTION

Laser beaming is the one of the most efficient energy transmission methods in space. Therefore, in the near future, a laser energy network similar to the one schematically shown in Fig. 1 is expected to be realized in space. Either solar or nuclear power stations will provide energy to satellites, space platforms and even space vehicles, depending on the energy demand. Laser propulsion will work as an efficient energy converter from laser energy to kinetic energy.

Our research is focused on propulsion involving a CW laser, in which physical phenomena are expected to be stationary and easy to handle compared with

*Graduate Student, Department of Aeronautics and Astronautics.

†Associate Professor, Department of Advanced Energy, Member AIAA.

‡Professor, Department of Aeronautics and Astronautics, Member AIAA.

those concerning propulsion using repetitively pulsed laser devices. Several experimental studies have been carried out on this so-called CW laser propulsion, measuring both the laser absorption fraction and the thrust,³⁻⁸⁾ from which the performance characteristics were revealed. However, this experimental approach is quite limited because high power laser devices are very expensive and, furthermore, carrying out diagnostics of the plasma inside of the laser thruster is a very difficult task. Therefore analytical studies are also very important. In previous research⁹⁻¹³⁾, detailed physical models were constructed and validated against experimental data. However, as it will be described later, in order to avoid computational difficulties encountered in multidimensional simulations, some authors have approximated or simplified their models by either adding artificial viscosity to the scheme¹⁰⁾, ignoring flow in the radial direction^{11,12)}, or assuming the flow to be subsonic in the entire flowfield¹³⁾. In this study, an efficient CFD code is employed in order to simulate the propellant heating processes induced by a laser beam inside of a thruster without ignoring the flowfield characteristics.

Since laser thrusters will fly leaving energy sources on the ground, the exhaust velocity (or specific impulse) becomes of importance as well as the energy conversion efficiency. In order to increase the exhaust velocity, higher laser power should be absorbed using less propellant gas by optimizing the laser absorption location in the thruster chamber.

In general, the plasma produced by laser heating is called a Laser Sustained Plasma. The LSP is located at the position where the laser absorption rate is balanced by the energy dissipation rate towards the low temperature surrounding gas. The dominant physical phenomena dictating this energy balance inside of the thruster are the laser beam optics, inverse bremsstrahlung absorption, ionization/recombination reactions, radiation loss, heat conduction and convection. If a numerical code can predict the LSP position properly, it can be utilized to optimize the thruster geometry and to assess the performance of full-scale thrusters. Therefore, it is quite important for the code to be able to accurately predict the LSP position.

In addition, it is necessary to understand the energy dissipation mechanisms in order to improve the thruster performance. To this respect, the analytical study is considered to play a very important role, along with the experimental study

2. PHYSICAL MODEL

2.1. Laser Intensity Distribution

Assuming that a 0th order Gaussian laser beam is passing through a converging lens and focused inside of a chamber, the laser intensity distribution is given by

$$I(x, y) = \frac{2}{\pi} \frac{P}{w(x)^2} \exp\left(-\frac{2y^2}{w(x)^2}\right) \quad (1)$$

Here, $w(x)$ is the beam spot radius where the intensity drops to $1/e^2$ center intensity on the axis. It varies depending on the axial distance from the focus as

$$w(x) = w_f \sqrt{1 + \left(\frac{\lambda(x - x_f)}{\pi w_f^2}\right)^2}, \quad w_f = \frac{2f\lambda}{\pi w_0} \quad (2)$$

Even if lens aberration is ignored, finite beam waist w_f exists at the focal point due to the beam diffraction. Owing to the laser absorption by plasma, the beam intensity distribution differs from being Gaussian. This is taken into account by having the laser beam divided into 2400 bundles of rays and applying Beer's law to each ray.

$$\frac{dI_n}{dx} = -KI_n \quad (3)$$

By integrating Eq. (3), the average absorption rate inside of a cell having the width Δx along each ray is expressed as

$$q = \sum_n I_n(x, y) \frac{(1 - \exp(-K\Delta x))}{\Delta x} \quad (4)$$

Beam diffraction may take place on the boundary of LSP. Because of this, compared to the case with no plasma, the beam waist is thought to be about 10 times larger. However, this effect is small in the case when there is little absorption in the vicinity of the focus. Therefore, diffraction effects are not considered here. Although some percentage of the transmitted light and the radiation from plasma is reflected on the wall surfaces of the chamber, this effect is assumed negligibly small.

Since the CO₂ laser used in the experiments is for material processing, although the intensity distribution is mainly a 0th order Gaussian, its central part exhibits several bumps in the distribution. As an approximation to the actual beam distribution, a beam diameter including 97.5 % of the total energy is made to exhibit a Gaussian distribution. From the beam profile measurements, the beam diameters were 34 mm and 30 mm for laser powers of 400W and 700W respectively. The corresponding f values (= focal length / beam diameter) were 7.35 and 8.33 respectively. (The focal length of the convex lens is 250 mm.)

2.2 Inverse Bremsstrahlung Absorption.

The propellant gas considered in the present analysis is argon. The absorption coefficient K_{EI} for electron inverse bremsstrahlung is a function of wavelength and temperature. Using the expressions given by Kemp⁹⁾ we have,

$$\frac{K_{EI}}{\rho_p^2} = \frac{1.37 \times 10^{-27}}{T^{1/2} M^2} \lambda^3 G \left(\exp\left(\frac{0.014388}{\lambda T}\right) - 1 \right) \quad (5)$$

with the Gaunt factor G being,

$$G = 1.04 + 3.74 \times 10^{-5} T - 3.28 \times 10^{-10} T^2 \quad (6)$$

The absorption coefficient K_{EN} for electron-neutral particle inverse bremsstrahlung is obtained also from Kemp⁹⁾ as,

$$\frac{K_{EN}}{\rho_p \rho_n} = \frac{9.6 \times 10^{-5}}{M^2} T^2 A(T) \lambda^3 \left(1 - \exp\left(\frac{-0.014388}{\lambda T}\right) \right) \quad (7)$$

where $A(T)$ is smoothly-varying and temperature-dependent coefficient.¹⁴⁾ The coefficients used in the present work are plotted in Fig. 2.

2.3. Ionization and Recombination Reactions

Singly ionized argon is considered. Since the flow speed in the chamber is quite slow, the gas must be in thermochemically equilibrium. Therefore, Saha's equilibrium equation holds, written as

$$\left(\frac{n_p n_e}{n_n} \right) = \left(\frac{2g_+}{g_0} \right) \left(\frac{2\pi m k T}{h^2} \right) \exp\left(\frac{-e\epsilon_i}{kT}\right) = 2 \left(4 + 2 \exp\left(\frac{-2062}{T}\right) \right) 2.4 \times 10^{21} T^{\frac{3}{2}} \exp\left(\frac{-1.81 \times 10^5}{T}\right) \quad (8)$$

Using this expression, the dependence of various physical constants (absorption coefficients, radiation strength, etc.) on pressure and degree of ionization is taken into account. However, in

calculating ionization and recombination reactions in the flow, the formulation with finite reaction rates is convenient for our implicit scheme. Therefore, the following ionization rate is used.

$$\omega_f = 1.15 \times 10^{27} T^{-3} \exp\left(1.81 \times 10^5 / T\right) \quad (9)$$

The recombination rate can be given from the principle of detailed balance coupled with Saha's equation as

$$\omega_b = (1/M) (n_n / n_p n_e) \omega_f \quad (10)$$

The energy equation is defined by considering the ionization energy as the enthalpy for plasma formation and is given by,

$$E = \frac{P}{\gamma - 1} + \frac{1}{2} \rho (u^2 + v^2) + \rho_p h_p \quad (11)$$

The specific heat ratio is assumed 5/3.

2.4. Radiative Losses

In a laser thruster, the radiative loss is considered to be a predominant energy loss mechanism. Many radiation intensity measurements have been carried out at atmospheric pressure,^{15,16)} and all of the results show similar temperature-dependence characteristics. In this work, the temperature-dependence is taken from Emmons data¹⁵⁾. The pressure-dependence, however, is an unknown factor. Since the radiative loss is theoretically thought as proportional to the product of the electron and ion number densities, the pressure-dependence is taken into account by using Saha's equation.

2.5. Heat Conduction

The thermal conductivity for argon gas rises once the plasma generation starts, because of a large contribution from the electrons. The electron thermal conductivity values for weakly ionized plasmas are given by Devoto.¹⁹⁾ As the plasma diffuses to the low temperature regions, recombination occurs and then the heat is locally generated, resulting in energy transport. This transport phenomenon is considered by calculating explicitly the diffusion and the ionization/recombination reactions. The following ambipolar diffusion coefficient for argon is used.

$$D \cong \frac{2kT}{M\nu} = 4.32 \times 10^{-6} T^{1/2} / (\rho_n + \rho_p) \quad (12)$$

As shown in Fig. 4, the theoretical and experimental values for thermal conductivity differ as the temperature increases. This discrepancy is due to the short wavelength radiation emanating from the plasma that is again absorbed in the low temperature region and released as thermal energy. This heat transfer, appearing in the form of radiation, can be approximated with Fourier's formulation, giving the heat flux proportional to the temperature gradient⁹.

The radiative thermal conductivity phenomenon can be deduced from many experimental results. Also, as the size of plasma becomes larger, this heat transfer tends to increase.¹⁹ To this respect, in this work the experimental results given by Emmons¹⁵ (the plasma radius $R = 5$ mm) are employed, assuming that the conductivity is proportional to the plasma radius (Herein $R = 1$ mm).

2.6. Convection

Since the propellant is choked at the throat, compressibility effects are important in the vicinity of the throat. In addition, inside of the chamber the temperature rises due to the heating by the laser beam, and sharp density drops are present in the flow. Therefore, it is necessary to consider compressibility in the whole flowfield.

In compressible flows, information propagates at the sonic speed and a limit on the calculation time-step exists. Namely, the Courant number cannot be greater than unity. When low Mach number flows, with $M = 0.01$ or smaller, are predominant in the chamber, a very large number of iterations are necessary in order to obtain numerical convergence. However, with an implicit method the maximum theoretical time-step can be infinite, thus circumventing the stiffness present in the equations. In practice, when attempting to carry out the necessary matrix inversions or making the physical constants vary depending on the characteristic variables, it becomes very difficult to make the scheme completely implicit. The time-step sets a limitation on the upper bound of the Courant number. It is noted that preconditioning the Jacobian matrices in order to speed up numerical convergence is a method being investigated by several authors⁶.

3. NUMERICAL METHOD

3.1. Governing Equations

In the basic system of equations, compressibility and energy diffusion are considered, employing the axisymmetric Navier-Stokes equations. In cylindrical coordinates, the system is given by,

$$\frac{\partial U}{\partial t} + \frac{\partial F_1}{\partial x} + \frac{\partial y G_1}{y \partial y} - \frac{\partial F_v}{\partial x} - \frac{\partial y G_v}{y \partial y} = W \quad (13)$$

where

$$U = \begin{bmatrix} \rho_n \\ \rho_p \\ \rho u \\ \rho v \\ E \end{bmatrix}, \quad F_1 = \begin{bmatrix} \rho_n u \\ \rho_p u \\ \rho u^2 + p \\ \rho uv \\ (E + p)u \end{bmatrix}, \quad G_1 = \begin{bmatrix} \rho_n v \\ \rho_p v \\ \rho uv \\ \rho v^2 + p \\ (E + p)v \end{bmatrix},$$

$$F_v = \begin{bmatrix} 0 \\ 0 \\ \tau_{xx} \\ \tau_{xy} \\ \tau_{xx}u + \tau_{yy}v + \kappa \theta_x T \end{bmatrix}, \quad W = \begin{bmatrix} -\omega_f \rho_p \rho_n + \omega_b \rho_p^3 \\ \omega_f \rho_p \rho_n - \omega_b \rho_p^3 \\ (p - \tau_{\theta\theta})/r \\ 0 \\ q \end{bmatrix} \quad (14)$$

The equation of state is given by,

$$p = (\rho_n + 2\rho_p)RT \quad (15)$$

An upwind discretization method called Flux Vector Splitting²⁰ is employed and the governing equations are solved implicitly using a Gauss-Seidel line relaxation method²¹. This overall method is characterized by its robustness and allows large Courant numbers.

3.2. Boundary and Initial Conditions

At the inlet, the total temperature, pressure and one more variable are obtained using an upcoming Riemann invariant. At the outlet, the supersonic exit condition is chosen, and at the wall, the adiabatic and slip conditions are used.

Although the viscosity on the wall has some effect on the choked flux, solving for the boundary layer directly would pose very intensive computational demands, and thus it is not considered in the present work.

In general, applying a CW laser beam of a 2kW level on a gas at room temperatures does not generate plasma, and so at first it is necessary to create a high temperature region artificially along the laser beam path wherein weak ionization will take place. The location where the plasma is first ignited has no effect on the steady-state computational results. As for the

experiments, a tungsten rod is often inserted into the chamber to induce ignition^{8,22}).

3.3. Calculated Conditions

Incoming laser beam powers of 400W or 700W are considered, with a laser wavelength of 10.6 μm . In order to simulate the experiments using our laboratory-model thruster, the throat diameter is set to 1mm and the half-cone angle of the converging part of the nozzle is set to 20 degrees. The total temperature is chosen as 300 K and the mass flow is either 1.2 or 0.9 g/s.

As for the spatial accuracy of the numerical discretization, a MUSCL approach was employed. A third order upwind differencing is used for the convective terms, and a fourth order central differencing is used for the viscous terms. The calculation is carried out with Courant numbers of 100~300.

3. CALCULATION RESULTS

4.1. Computational Grid and Grid Dependence

The computational grid is shown in Fig. 5. In order to check the grid independence, we tested several grid spacings in the radial direction which is important for accurate computation of the radial heat conduction. For the case with $P=700\text{W}$ ($f=8.33$) and a mass flow rate of 1.2 g/s, the grid-dependence characteristics as given by the maximum temperature and laser absorption are shown in Fig. 6. If the grid spacing Δy is less than 0.1 mm, the introduced error for the values of the maximum and the laser absorption is found to be kept within 1%. Therefore, the 150 x 50 grid employed in the present work is deemed appropriate. If the value of f is smaller, the LSP location shifts closer to the focus. Then, sudden changes in the streamlines take place in front of the LSP with vortices appearing in the flow. To resolve such complicated flow, a more refined mesh becomes necessary.

4.2. Two Dimensional Distribution

Typical contours of the temperature and degree of ionization are plotted in Fig. 7. The dashed line in the figure represents the boundary where the laser power

intensity becomes $1/e^2$ center intensity. In this figure, the focus is 10 mm downstream from the throat. The LSP is generated about 20mm upstream from the focus. The maximum temperature is of around 15000K and the degree of ionization is around 4%. In the vicinity of the throat, plasma has completely recombined but a relatively high temperature is maintained. The estimated average total temperature of the exhaust gas is around 1200K, which is four times larger than the temperature at the inlet. In order to obtain a high specific impulse, it is necessary to either bring the LSP closer to the throat or to increase the laser power.

The propellant gas flow close to the wall surface does not get heated at all. Therefore, the adiabatic wall condition is deemed appropriate under these operating conditions.

Plots of the streamlines and velocity vectors in the chamber and nozzle regions are given in Fig. 8. The streamlines are forced to continue around the LSP due to a slight pressure rise in front of the LSP. As a result, the flux passing through the inside region of the LSP is only 2~3% of the whole flux. The rest of the propellant gas is by the heat conduction from the LSP. In other words, it can be stated that the LSP plays the role of a heater.

Turning now to the flow inside of the nozzle, in the vicinity of the central axis the flow velocity in the high temperature region differs greatly from the one in the surrounding low temperature region. Only the propellant gas passing through the inside of the LSP has a large exhaust velocity. Owing to this, the energy conversion efficiency η_T based on the thrust is poor, compared to the energy conversion efficiency η_E based on the total sum of the kinetic energy of each particle.

Here, the energy conversion efficiency based on the thrust T is defined as,

$$\eta_T = (T^2 - T_g^2) / 2\dot{m}P \quad (16)$$

On the other hand, the energy conversion efficiency estimated from the total sum of the kinetic energy of each particle is,

$$\eta_E = \int (\rho V_j^2 / 2 - \rho_g V_{jg}^2 / 2) 2\pi r dr / P \quad (17)$$

In the case of expansion into a vacuum, if the energy diffusion in the expansion process is ignored, the laser absorption efficiency (η) = (Laser absorption -

Radiative loss) / Incident Laser Power) is equal to the energy conversion efficiency $\eta_{E\infty}$ (the ultimate energy conversion efficiency).

4.3. Comparison with Experimental Results

A diagram of the device used in the experiments is shown in Fig. 9. A 2-kW laser is employed. The laser beam diameter is magnified to about 30mm with a beam expander, and then using a ZnSe focusing lens (focal length =250mm) the beam is focused inside of the thruster chamber. The position of the focus can be controlled by moving the focusing lens with a stepping motor. The LSP is viewed through the observation window located on a side of the chamber using a CCD camera.

Argon is used as the propellant gas. The chamber is designed to withstand pressures up to 10 atm, and this chamber pressure varies depending on the mass flow rate regulation. In the experiments, the thrust, chamber pressure and the heat lost to the walls are all measured. A simple thrust stand equipped with a load-cell sensor is utilized to measure the thrust. Since the thrust is measured under atmospheric pressure, it is thought that the flow is over-expanded at the nozzle exit and flow separation occurs. As for the chamber pressure, the static pressure was measured via the pressure port located on a side of the chamber. Since flow Mach number in the chamber is expected around 0.01, the static pressure is taken as the total pressure. The heat loss is estimated by measuring the temperature difference between inlet and outlet of the cooling water pipe.

A photograph of the LSP is shown in Fig. 10, using filters that reduce luminosity by a factor of 1/1000. The size of LSP is 2mm in the flow direction and 1mm in the radial direction. Detailed measurements - such as temperature distributions inside of the thruster- have not been carried out yet.

The distance from the focus to the center of the LSP varies depending on the magnitude of the laser power and the position of the focus. When the focus moves closer to the throat, the LSP location shifts closer to the throat and if it moved further, the LSP is sucked in down the throat and decreases in size. This is possibly due to the changes in local laser intensity, local flux density and so on, in a unit cross section for a given position in the axial direction.

The comparison between the calculated and measured center positions of LSP is shown in Fig. 11. In order to define the LSP region in the calculation, the contour where the degree of ionization is 2% is taken as the LSP boundary. In both calculation and measurement, the LSP is generated 8~10 mm downstream of the focus in the $P = 400W$ case and 18~20 mm downstream of the focus for the $P = 700W$ case. Also, as the focus is moved downstream, good agreement is obtained in predicting the tendency for the distance between the LSP and the focus to become smaller. Therefore, it can be said that the coupling of the laser absorption and convection phenomena is well reproduced in the present simulation code.

By further increasing in the laser power, the distance between the LSP and the focus becomes larger, and the LSP cannot be maintained at the region near the observation window. Conversely, by decreasing the laser power below 300W, in both the experiments and the computation the plasma could not be sustained. Although experiments varying the f value have not been performed, in the calculation it was observed that by making f smaller the LSP is brought closer to the focus. This way, a higher laser power can be applied without having the LSP running too far upstream, which is undesirable. In this case, vortices appear inside of the chamber, although they have no effect on the thruster performance.

4.4. Energy Conversion Efficiency

In the experiment, the measured thrust agreed well with the one estimated by assuming proper expansion of the propellant gas from measured chamber pressure to atmospheric pressure. This suggests that the thrust obtained using the thrust coefficient as,

$$T = C_F p_c (\pi D_t^2 / 4) \quad (18)$$

provides a very close approximation, where

$$C_F = \sqrt{\frac{2\gamma^2}{\gamma-1} (2/(\gamma+1))^{\gamma+1/(\gamma-1)} (1 - (p_e/p_c)^{\gamma-1/\gamma})} \quad (19)$$

Herein p_e is the atmospheric pressure. In the case of expansion to a vacuum, the thrust can be calculated by just setting $p_e = 0$.

As for the computation, since the grid in the nozzle region is too coarse to allow accurate estimation of the velocity variation, instead of calculating the thrust

by integrating the momentum over a given cross sectional surface, it is estimated via Eqs. (18) and (19) Values for the thrust and the energy conversion efficiency from the experiment and the computation are listed in Table 1. The mass flow rates were the same. To obtain the energy conversion efficiency, the code was run without laser heating. Finally, the code was also run for the case where the laser thruster operates in a vacuum, yielding the ultimate conversion efficiency.

4.5. Energy Balance

Energy balances based on the data given in Table 1 are shown in Fig. 12. The ultimate energy conversion efficiency based on the thrust is around 16% in both the experiment and the calculation. Since the calculated laser absorption efficiency is 23%, there is a 7% gap between these efficiencies. This gap is considered to be from the non-uniformity in the velocity distribution of the exhaust jet as shown in Fig. 9. The same amount of energy loss would exist as non-recovered energy loss in the experiment.

The laser energy not absorbed by the propellant gas and the radiation energy from the plasma fill the inside of the chamber as so-called photon energy. Part of this energy is absorbed on the wall surface and becomes heat loss. The remaining energy is thought to either cross on to the inlet window or travel down the throat.

Using the measured heat loss fraction to the wall surface, it is estimated that 56% of the transmitted light and radiated light is absorbed by the wall surface and the remaining 44% is lost to the outside of the chamber.

This photon energy loss is thought to be a predominant energy loss mechanism in the laser thruster. Therefore, it would be desirable to reduce the release of this energy to the outside and recover some of it using regenerative cooling, so as to improve the efficiency as well as the specific impulse.

5. CONCLUSIONS

A numerical model to analyze the LSP behavior, dominated by six physical phenomena (laser beam optics, inverse bremsstrahlung absorption, ionization/recombination reactions, radiation, heat

conduction, and convection) has been developed. The problem of stiffness in the system of equations has been circumvented using a stable implicit scheme allowing large time-steps.

The computed LSP position agrees well with the experimental results. This implies that the present physical model and aerodynamic code are suitable for accurate prediction.

Finally, the energy balance obtained from the numerical analysis provide a new viewpoint when interpreting experimental results, and provide knowledge necessary to further improve thrust performance.

REFERENCES

- 1) Kantrowitz, A.: Propulsion to Orbit by Ground-Based Lasers, *Aeronautics and Astronautics*, Vol. 10 (1972), pp. 74-76.
- 2) Bitat, M.A.: Laser Propulsion: Research Status and Needs, *J. Propulsion and Power*, Vol. 8, No. 2 (1992), pp.354-360.
- 3) Mead, F.D., Myrabo, L.M., and Messitt, D.G.: Flight and Ground Tests of a Laser-Boosted Vehicle, AIAA Paper 98-3735, Cleveland, OH, 1998.
- 4) VanZandt, D.M., McCay, T.D., and Eskridge, R.H.: An Experimental Study of Laser Supported Hydrogen Plasmas, AIAA Paper 84-1572, Snowmass, CO, 1984.
- 5) Keefer, D., Welle, R., and Peters, C.E.: Power Absorption in Laser-Sustained Argon Plasma, *AIAA J.*, Vol. 24, No. 10 (1986), pp. 1663-1669.
- 6) McMillin, B.K., Zerkle, D.K., Glumb, R.J., Krier, H., and Mazumder, J.: Energy Conversion in Laser Sustained Argon Plasmas for Application to Rocket Propulsion, AIAA Paper 87-1459, Honolulu, Hawaii, 1987.
- 7) Schwartz, S., Mertogul, A., Eguiguren, J., Zerkle, D., Chen, X., Krier, H., and Mazumder, J.: Laser-Sustained Gas Plasmas for Application to Rocket Propulsion, AIAA Paper 89-2631, Monterey, CA, 1989.
- 8) Black, J., Krier, H., and Glumb, R.J.: Laser Propulsion 10-kW Thruster Test Program Results, *J. Propulsion and Power*, Vol. 11, No. 6 (1995), pp.1307-1316.

9) Kemp, N.H. and Lewis, P.F.: Laser-Heated Thruster – Interim Report, NASA CR 161665, 1980.
10)Jeng, S-M, Litchford, R., and Keefer, D.R.: Computational Design of an Experimental Laser-Powered Thruster, NASA CR 183587, 1988.
11)Glumb, R.J. and Krier, H.: Two-Dimensional Model of Laser-Sustained Plasma in Axisymmetric Flowfields, *AIAA J.*, Vol. 24, No. 8 (1986), pp. 1331-1336.
12)Girard, M., Lebehot, A., and Campargue, R.: Numerical Simulation for the Generating Conditions of a Laser Sustained Argon Plasma Jet, *Phys. D: Appl. Phys.* 27 (1994), pp.253-262.
13)Molvik, G.A., Choi, D., and Merkle, C.L.: A Two-Dimensional Analysis of Laser Heat Addition in a Constant Absorptivity Gas, *AIAA J.*, Vol. 23, No. 7 (1985), pp. 1053-1060.
14)John, T.L.: The Free-Free Transitions of Atomic and Molecular Negative Ions in the Infrared, *Mon. Not. R. Astr. Soc.*, Vol. 170, No.1 (1975), pp.5-6.
15)Emmons, H.W.: Arc Measurement of High-Temperature Gas Transport Properties, *Phys. Fluids*, Vol. 10, No. 6 (1967), pp. 1125-1136.
16)Owano, T.G., Gordon, M.H., and Kruger, C.H.: Measurements of the Radiation Source Strength in

Argon at Temperatures between 5,000 and 10,000 K, *Phys. Fluids B*, Vol. 2, No. 12 (1990), pp. 3184-3190.
17)Kozlov, G.I., Kuznetsov, V.A., and Masyukov, V.A.: Radiative Losses by Argon Plasma and the Emissive Model of a Continuous Optical Discharge, *Sov. Phys. -JETP*, Vol. 39, No. 3 (1974), pp. 463-468.
18)Oettinger, P.E. and Bershader, D.: A Unified Treatment of the Relaxation Phenomenon in Radiating Argon Plasma Flows, *AIAA J.*, Vol. 5, No. 9 (1967), pp. 1625-1632.
19)Candler, G.V., MacCormack, R.W.: The Computation of Hypersonic Ionized Flows in Chemical and Thermal Nonequilibrium, *J. Thermophysics and heat transfer*, Vol. 5, No. 3 (1991), pp. 266-273.
21)MacCormack, R.W.: Current Status of the Numerical Solutions of the Navier-Stokes Equations, AIAA Paper 85-0032, Reno, NV, 1985.
22) Toyoda, K., Komurasaki, K., Arakawa, Y.: An Experimental Research on a CW CO₂ Laser Thruster, 26th Inter'l Electric Propulsion Conf., IEPC 99-012, Kitakyushu, Japan, 1999.

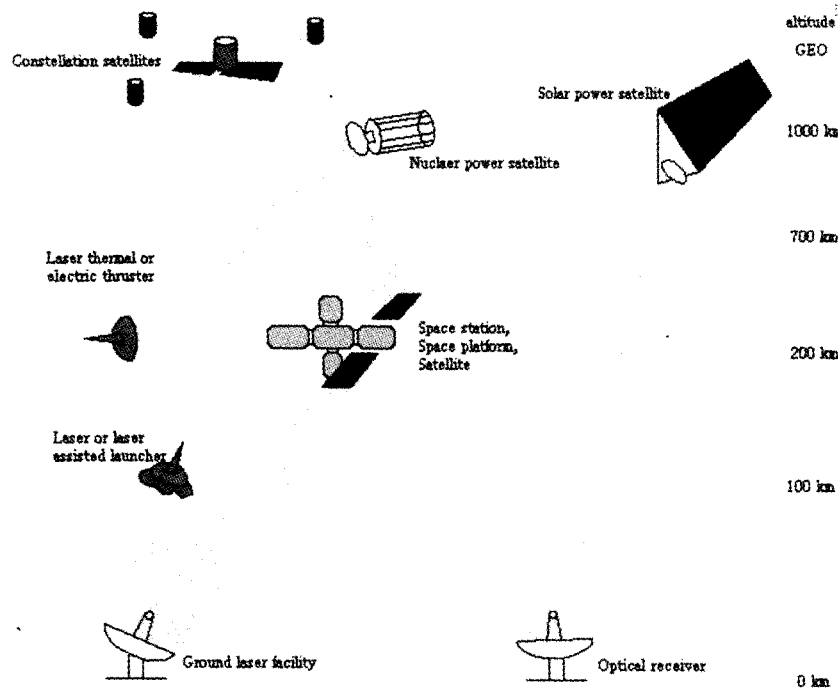


Fig. 1 Laser Energy Transmission Network

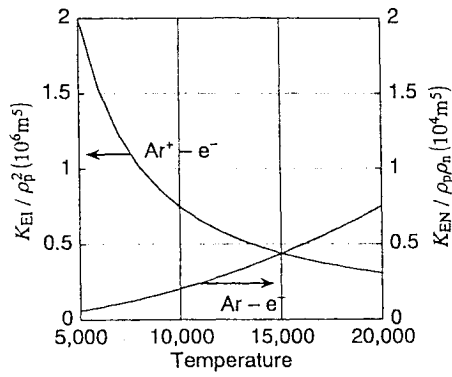


Fig. 2 Absorption Coefficients

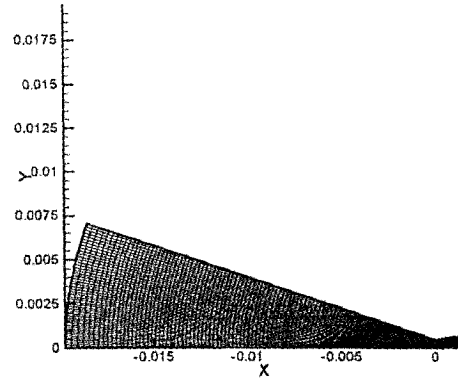


Fig. 5 Computational Grid

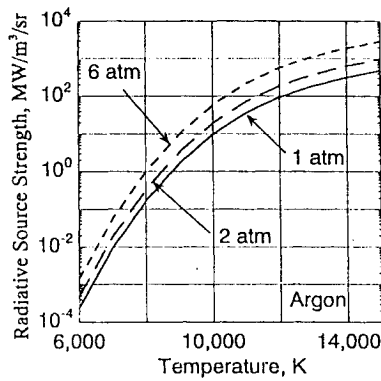


Fig. 3 Radiative Source Strength

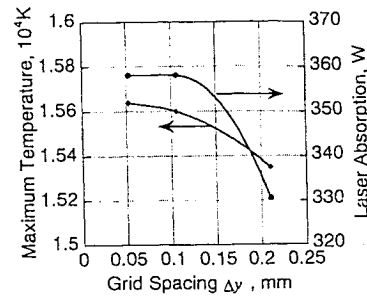


Fig. 6 Grid Dependence

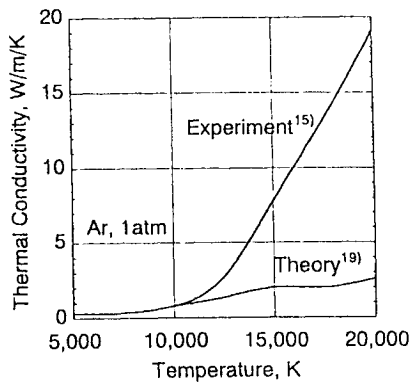


Fig. 4 Thermal Conductivity

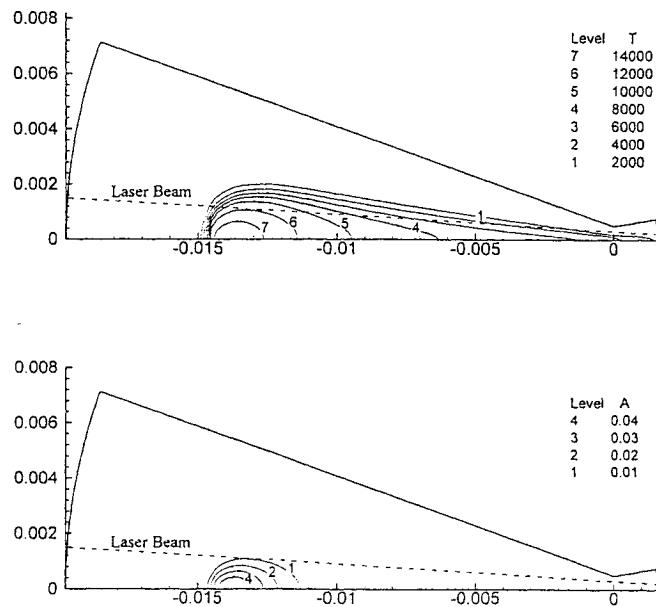


Fig. 7 Temperature Countours (above) and Degree of Ionization Contours (below)

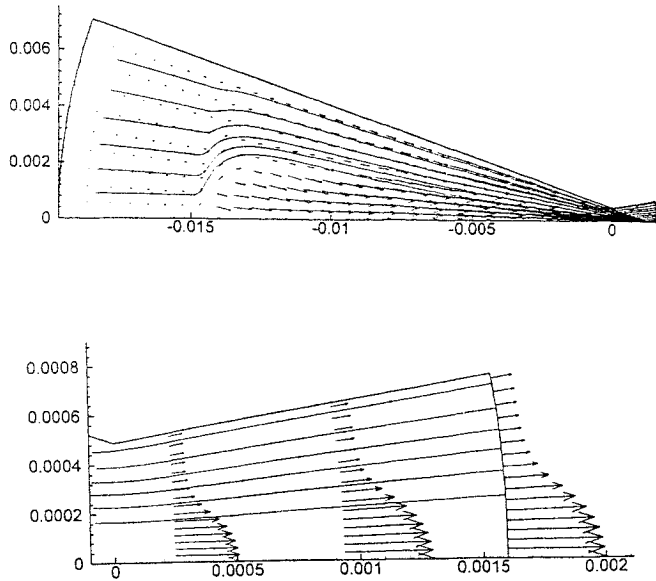


Fig. 8 Flowfield Streamlines and Velocity Vectors in the Chamber (above) and Nozzle (below)

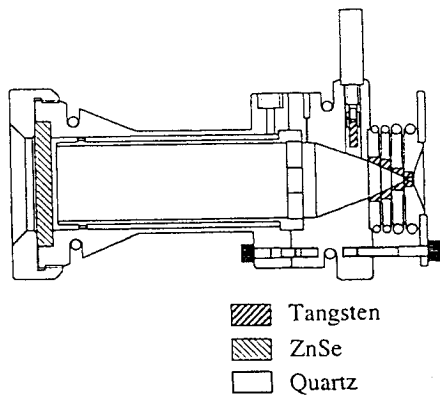


Fig. 9 Laboratory Thruster

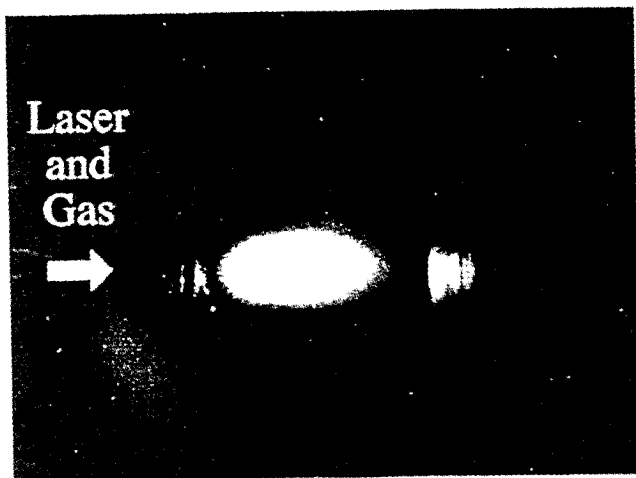
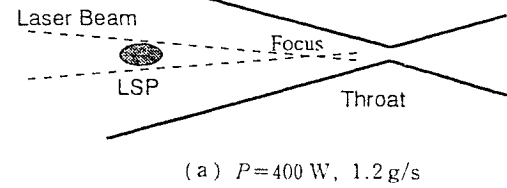
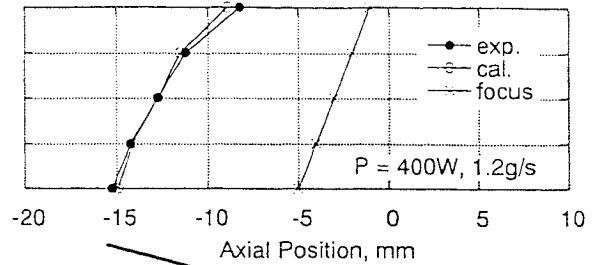
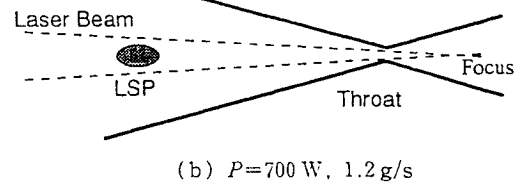
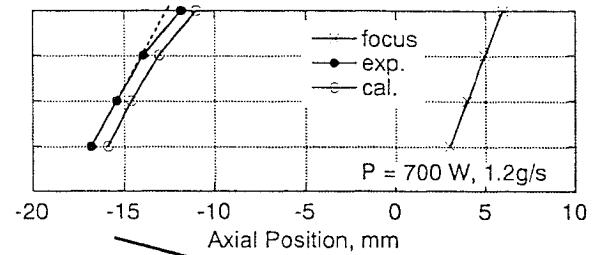


Fig. 10 LSP Photograph



(a) $P = 400\text{ W}$, 1.2 g/s



(b) $P = 700\text{ W}$, 1.2 g/s

Fig. 11 Focus and LSP Locations for $P = 400\text{ W}$ (above) and $P = 700\text{ W}$ (below)

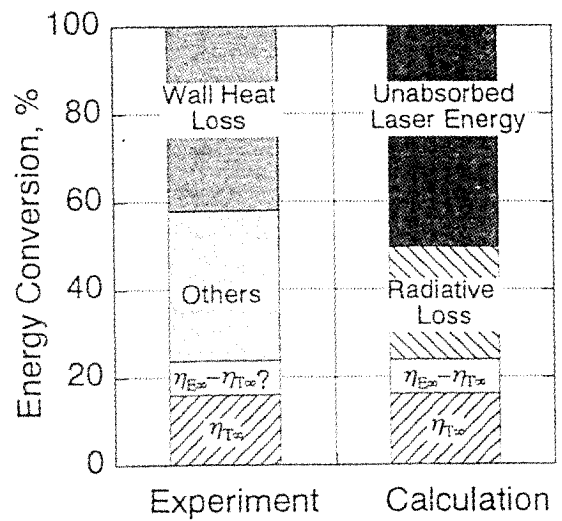


Fig. 12 Energy Distribution

Table 1. Thrust and Energy Conversion Efficiency

	Experiment	Calculation
Chamber Pressure,		
P_c (KPa)	534	534
T/T_∞ (mN)	454/681	475/681
Chamber Pressure		
P_{cg} (KPa)	403	404
$T_g/T_{g\infty}$ (mN)	324/513	336/515
$\eta_T/\eta_{T\infty}$ (%)	8.1/16.1	9.0/15.9